ADVANCED MATERIALS
www.advmat.de

Bioinspired Hierarchical Radiative-Phase Change Hybrid Cooling Composite with Record-Breaking Cooling Power

Xinpeng Hu, Bingqing Quan, Zhanjin Shi, Xiangyu Zhao, Gangchen Lu, Yang Ding, Jiancheng Lai, Jinping Qu, Yucan Peng,* and Xiang Lu**

Passive daytime radiative cooling (PDRC) offers a sustainable route to reducing cooling energy consumption and greenhouse gas emissions. However, conventional PDRC materials exhibit limited cooling power (<150 W m^{-2}), insufficient for growing cooling demands. While integrating phase change materials enhances cooling capacity, to balance radiative cooling, latent heat, and heat transfer performances remains challenging due to their conflicting requirements. Inspired by the light scattering mechanism of nacre-pearl systems, hierarchically microstructured radiative-phase change hybrid cooling (RPHC) composites with a homogeneous morphology are developed via a water pre-removal strategy. The composite combines a multilayered microfibrillated cellulose (MFC) matrix with core–shell phase change capsules (PCCs), achieving solar reflectivity of 0.969 and mid-infrared emissivity of 0.958. Efficient PCC integration provides a high latent heat of 132.1 J g^{-1}. This nacre-pearl-inspired design enables a record-high PRHC power of 226 W m^{-2} and an average temperature reduction of 10.1 °C below ambient. Applied to building envelopes, the MFC/PCC composite reduces cooling energy use by up to 4.4%, potentially cutting global CO_2 emissions by 1.22 billion metric tons annually. Overall, this work provides innovative energy-saving materials for energy savings and carbon neutrality.

1. Introduction

As global warming intensifies, the frequency and severity of extreme heat waves have increased, posing substantial risks to both human health and economic stability.[1] Buildings, which serve as essential shelter for humans, consume ≈15% of primary energy for air conditioning.[2] Therefore, there is a growing need for energy-efficient cooling technologies that can reduce both building energy consumption and greenhouse gas emissions.[3] Passive daytime radiative cooling (PDRC), which emits thermal radiation through the atmospheric window (8–13 μm) to dissipate heat, represents a promising, eco-friendly solution for cooling.[4–6] Moreover, PDRC requires no energy input, offers a diverse selection of materials, is easy to install and shows environmental friendliness.[7–10]

Various innovative PDRC material designs, including photonic structures, hybrid metamaterial films,[11] cooling wood,[12] and structured polymer materials,[13–15] have been reported to achieve impressive cooling performance with simultaneously high reflectivity and emissivity. Strategies such as dual-transmittance windows,[16] and fluorescence emittance[17] have been introduced to further boost net cooling power.[18] However, the practical cooling power remains limited to below 150 W m^{-2}, despite the advances in optical properties.[19] Such cooling capability is insufficient to satisfy the surging cooling demand. Therefore, advanced cooling technologies are needed to provide superior cooling capacities to conventional radiative cooling.

Phase change materials (PCMs) absorb heat during their phase transitions, typically from solid to liquid states.[20,21] Their

X. Hu, B. Quan, Z. Shi, X. Zhao, G. Lu, Y. Ding, J. Qu, X. Lu
Key Laboratory of Material Chemistry for Energy Conversion and Storage
Ministry of Education
Hubei Key Laboratory of Material Chemistry and Service Failure and
Hubei Engineering Research Center for Biomaterials and Medical
Protective Materials
School of Chemistry and Chemical Engineering
Huazhong University of Science and Technology
Wuhan, Hubei 430074, P. R. China
E-mail: jpqu@hust.edu.cn; luxiang@hust.edu.cn

J. Lai
Tachin Technology Co., Ltd
Beijing 100094, P. R. China

J. Qu
National Engineering Research Center of Novel Equipment for Polymer Processing
Key Laboratory of Polymer Processing Engineering
Ministry of Education
School of Mechanical and Automotive Engineering
South China University of Technology
Guangzhou 510641, P. R. China

Y. Peng
Department of Energy and Resources Engineering
College of Engineering
Peking University
Beijing 100871, P. R. China
E-mail: yucan.peng@pku.edu.cn

The ORCID identification number(s) for the author(s) of this article can be found under https://doi.org/10.1002/adma.202510988

DOI: 10.1002/adma.202510988

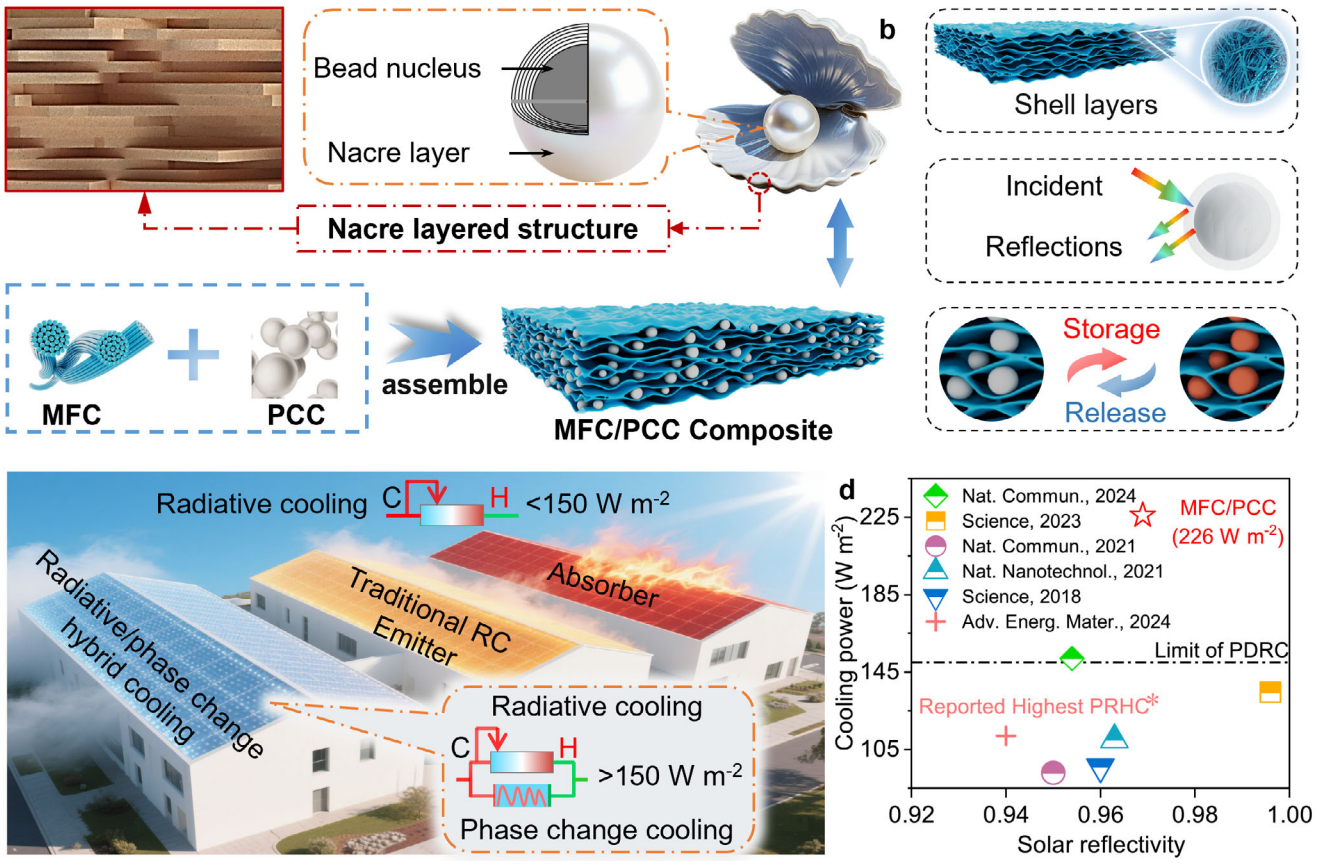

Figure 1. RPHC cooling design and its potential for building cooling energy saving. a) Design of bioinspired hierarchical RPHC composites. b) Working mechanism of RPHC composites. c) Illustration of the advantages of MFC/PCC composites. d) Comparison of MFC/PCC and conventional PDRC materials.[13–16,22,33]

latent heat absorption associated with these phase changes allows PCMs to remove excess heat during periods when conventional radiative cooling alone cannot satisfy the cooling demand, thus representing a promising approach to complement PDRC (Text S1, Supporting Information).[22–25] However, optimizing both radiative cooling and phase change performance simultaneously presents a significant challenge due to their inherently conflicting requirements. The conventional method to combine radiative cooling and PCMs involves coating a radiative cooling layer onto the surface of the phase change layer.[22,26] However, this approach faces limitations in efficiently transferring heat from the radiative cooling layer to the phase change layer, hindering the effectiveness of the phase transition. Consequently, the actual cooling performance of bifunctional phase-change composite film prepared by Wang et al. (average cooling power is less than 112 W m^{-2}) falls significantly short of the theoretical ideal value with high reflectivity (0.94) and emissivity (0.96).[22] An alternative approach is to integrate PCMs directly into PDRC materials to create a homogeneous composite that improves heat transfer.[27] Nevertheless, common PCMs, such as paraffin wax (PW) and polyethylene glycol (PEG), often pose leakage risks, and their low reflectivity or emissivity can compromise radiative cooling performance (highest cooling power of 89 W m^{-2} with latent heat of 88.3 J g^{-1}, Table S1, Supporting Information).[27–30] Besides, high-performance PDRC materials are typically porous,[17,31,32] which is critical for enhancing light scattering and achieving high solar reflectivity. The embedment of PCMs tends to decrease solar reflectivity due to possible disruption of the porous structure and the low refractive index contrast between PCMs and PDRC materials.[6] While coaxial electrospun fiber could be a good matrix to maintain the porous structure and keep PCM from leakage, it faces the limitation of low latent heat (always less than 100 J g^{-1}) in order to maintain excellent radiative cooling performance.[27] In summary, these methods are difficult to simultaneously achieve the requirements of reflectivity, latent heat, and heat transfer.

Nacre, a naturally occurring biomaterial, is renowned for its exceptional mechanical properties and sophisticated hierarchical structure. When pearls are embedded within the nacre, the surrounding regions remain visually bright – a phenomenon attributed to the synergistic enhancement of light scattering by both the layered nacre and the core–shell architecture of the pearls (**Figure 1a**). This nacre-pearl system exhibits pronounced counter-scattering effects due to the high refractive index contrast between the interface of the nacre-pearl system and the entrapped air, thereby significantly amplifying optical scattering efficiency. Inspired by this natural design, we hypothesized that encapsulating core–shell PCMs within a multilayered matrix

could simultaneously enhance solar reflectivity and PCM loading, thereby improving the overall cooling performance of PDRC systems.

Building on this concept, we developed a rapid water pre-removal strategy to fabricate a hierarchically microstructured radiative-phase change hybrid cooling (RPHC) composite with a homogeneous morphology (Figure 1b). This composite integrates a microfibrillated cellulose (MFC) matrix exhibiting self-assembled multilayered lamellae with well-distributed core–shell structured phase change capsules (PCCs). The resulting material achieves a high mid-infrared (MIR) emissivity of 0.958, while its porous morphology, coupled with the PCCs, contributes to a solar reflectivity of 0.969. Furthermore, the effective encapsulation of PCCs within the MFC network imparts a substantial latent heat capacity of 132.1 J g^{-1}, enabling efficient thermal energy storage and release.

As a result of the concurrent realization of high solar reflectivity, high MIR emissivity, elevated PCM loading, and robust latent heat capacity, the MFC/PCC composite delivers a record-high passive cooling power density of 226 W m^{-2} (Figure 1c,d). This value markedly exceeds those reported for conventional radiative cooling materials (typically <150 W m^{-2}) [13–16,22,33] and other RPHC composites. Notably, under direct solar irradiation, the composite can achieve a daytime temperature reduction of up to 10.1 °C below ambient. Energy modeling further demonstrates its substantial potential for building energy savings: when deployed on building roofs and façades across diverse climatic regions in China, the MFC/PCC composite enables reductions in cooling energy consumption by as much as 4.4%, offering both economic benefits and environmental gains through reduced greenhouse gas emissions.

2. Results

2.1. Design and Fabrication of the MFC/PCC Composite

The MFC/PCC composite was designed to simultaneously achieve several key attributes to maximize cooling power, specifically: i) a nacre-pearl inspired structure with high solar reflectivity and MIR emissivity, ii) high latent heat to enhance cooling capability, and iii) cost-effective materials and processing to achieve homogeneous heat transfer. To meet these objectives, we selected MFC and PCC as the primary components and developed a water pre-removal approach to fabricate the MFC/PCC composite, as illustrated in **Figure 2a**. We adopted the pre-filtration method to remove water to accelerate the drying process and control the structure of the obtained composite. The MFC was selected as the primary matrix material due to the multiple functional group vibrations that contribute to high MIR emissivity (Figure S1, Supporting Information) [13,34,35] and its intrinsic property to assemble to be a layered structure (Figure 2b). The PCM mimicking the pearl with the core–shell structure was introduced into the MFC matrix, providing additional phase change cooling power while preventing leakage. Specifically, melamine (with a high refractive index of n = 1.81) [36] and PW (with a low refractive index of n = 1.30) [37] were used as shell and core materials for the PCC, respectively (Figures S2 and S3, Supporting Information). Compared to PW alone, the core–shell PCC exhibits enhanced scattering efficiency in the solar spectrum, attributed to the enhanced scattering caused by the core–shell structure and impedance mismatches,[38–40] as demonstrated by Finite-Difference Time-Domain (FDTD) simulations (Figure S4, Supporting Information). This structure leads to enhanced sunlight scattering and a significant increase in reflected light. Additionally, the core–shell PCC shows a scattering spectrum closely aligned with the trend of the solar AM1.5 spectrum, indicating efficient scattering across a wide range of wavelengths.[14,38] Overall, the composition and structure of the PCCs enhance light scattering, thereby improving reflectivity. Notably, the shell thickness does not significantly affect scattering efficiency, highlighting the versatility of PCC preparation (Figure S5, Supporting Information).

The simple combination of MFC and PCC does not yield optimal optical properties. To achieve the desired performance, it is essential to regulate the composite structure, which was accomplished by adjusting the water content in samples before the freeze-drying process. By controlling the water filtration ratio while integrating PCCs with MFC, MFC/PCC composites with varied porous structures can be fabricated. The MFC/PCC composite, vacuum-filtrated to a dry state, is referred to as MFC/PCC-dry, while the MFC vacuum-filtrated to a dry state is termed MFC-dry. The remaining samples underwent both vacuum filtration and vacuum drying. During the vacuum filtration process, the proportion of water removed from the original water is called the water filtration ratio (20–90 wt.%). The corresponding resulting samples were designated as MFC/PCC-20 to MFC/PCC-90, respectively.

2.2. Optical Property and Phase Change Performance

When directly vacuum-filtrated to be dry, the MFC-dry forms a multilayered structure naturally after the vacuum filtration process owing to the intrinsic self-assembly behavior of MFC (Figure 2b). The MFC/PCC-dry exhibits a dense microstructure due to the crowding of MFC and PCCs, which limits the pore formation and causes the loss of spherical shape in the PCCs (Figure S6, Supporting Information). This structural disruption hinders light scattering, leading to a limited solar reflectivity of 0.478 (Text S2 and Figure S7, Supporting Information). In contrast, when 90% of water is removed by vacuum filtration before freeze-drying, MFC/PCC-90 shows markedly enhanced reflectivity (0.851) by promoting the formation of a porous structure and preserving the spherical morphology of PCCs within the MFC matrix (Figures S7 and S8, Supporting Information). At this water content, MFC self-assembles into a nacre-like structure to surround the PCC (Figure 2c,d). Solar reflectivity initially improves as the removed water ratio decreases (from full drying to 60% removal), but further reductions (from 60% to 20%) result in a decline in reflectivity. The MFC/PCC-60 owns the most homogeneous morphology with a bioinspired microstructure (Figures S9 and S10, Supporting Information). Higher magnification images reveal a nacre-pearl-like arrangement, in which spherical PCCs act as "pearls" embedded in a nacre-like MFC matrix (Figure 2c). The PCCs retain their spherical shape, which is important for effective light scattering. These nacre-pearl domains are located within larger pores, creating a distinct hierarchical microstructure, which explains the high solar reflectivity. Besides, the pore size distribution of MFC/PCC-60 peaks at 174 nm (Figure 2e),

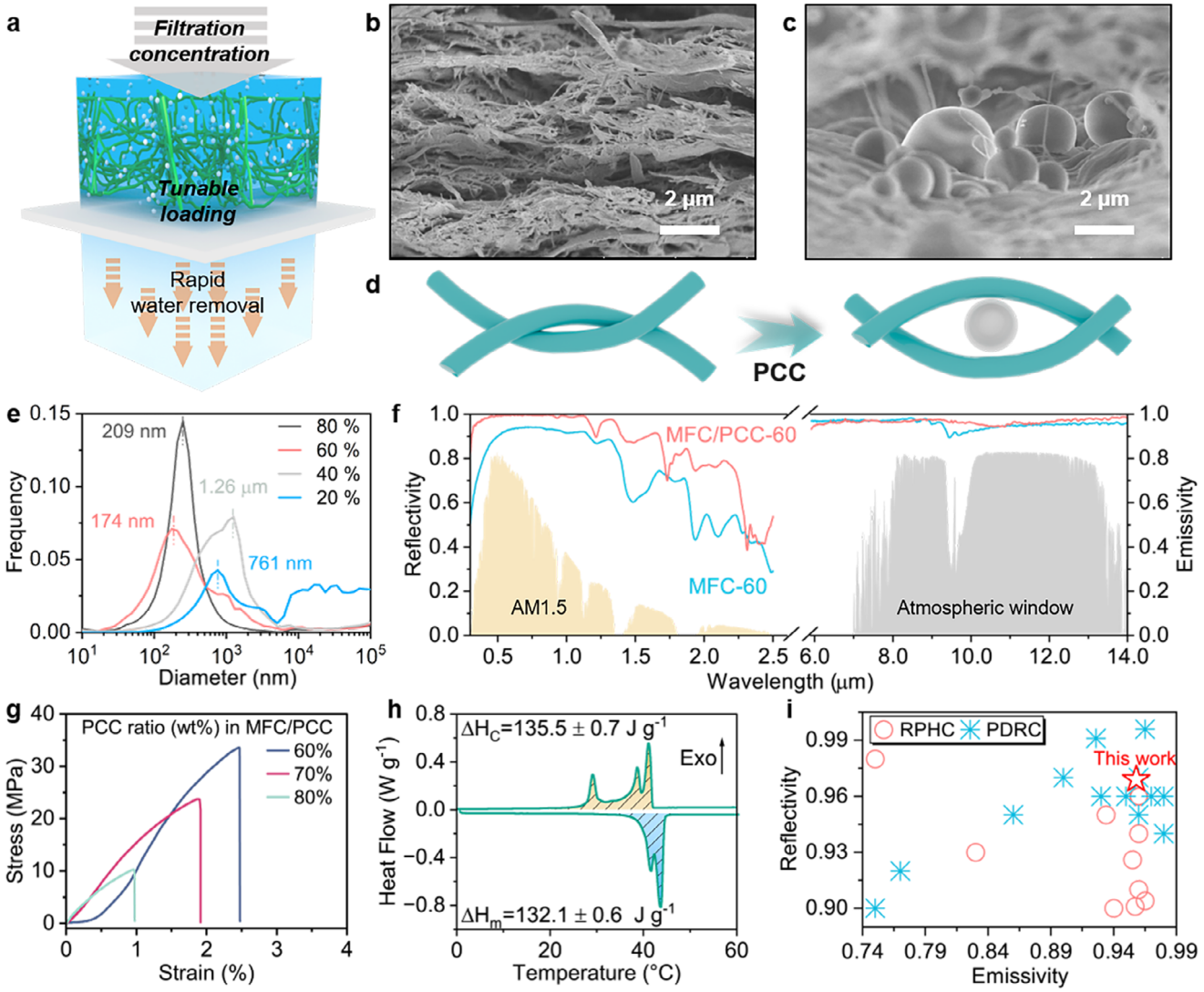

Figure 2. Optical and phase change properties of MFC/PCC composite. a) Fabrication illustration of MFC/PCC with water pre-removal freeze-drying. b) SEM image of MFC-dry. c)SEM image of MFC/PCC-60. d) Illustration of the fabrication difference between MFC-dry and MFC/PCC-60. e) The pore structure characterizations of MFC/PCC composite with varying water filtration ratio. f) The reflectivity and emissivity of MFC-60 and MFC/PCC-60. g) Mechanical performances of MFC/PCC with varying PCC weight ratios. h) The typical DSC curve and phase change parameters of MFC/PCC-60 with a heating and cooling rate of 1 °C min^{-1}. i) Comparison of MFC/PCC-60 with RPHC materials in the literature.

with the pore distribution aligning better with the AM1.5 solar spectrum, further enhancing scattering efficiency and reflectivity. However, when the water filtration ratio is further reduced to 40 wt.%, the peak pore size increases to 1.26 μm. A further reduction to 20 wt.% introduces non-uniform pore distribution, with a significant presence of pores exceeding 10 μm, likely due to structural defects,[41] as evidenced by the morphology of MFC/PCC-20 (Figure S9, Supporting Information). Optimally, the MFC/PCC-60 composite maintains a hierarchical porous structure and best preserves the spherical morphology for PCCs, yielding an exceptionally high reflectivity of 0.969.

The microstructural adjustments have a negligible impact on MIR emissivity (Figure S7, Supporting Information), with all MFC/PCC composite samples exhibiting high emissivity in the 8–13 μm atmospheric window. The emissivity values of MFC/PCC-20/30/40/50/60/70/80/90 and MFC/PCC-dry are 0.962, 0.955, 0.953, 0953, 0.958, 0.964, 0.973, 0.963, and 0.971, respectively. Overall, all the MFC/PCC samples achieved sufficiently high emissivity values.

We evaluated the effect of thickness on the reflectivity and emissivity of the MFC/PCC composite. Characterization of samples with varying thicknesses (100/400/800/1000 μm) revealed that the optimal reflectivity and emissivity for MFC/PCC appear at a thickness of 1000 μm, while further increasing the thickness from 800 to 1000 μm does not improve reflectivity and emissivity significantly (Figure S11, Supporting Information). Overall, both the introduction of PCCs and the adjustment of water content to construct a porous composite are effective strategies for optimizing optical performance especially the reflectivity (Figure 2f), as the incorporation of PCCs and hierarchical

nacre-pearl inspired microstructure markedly increases the scattering interface. The MFC/PCC achieved both remarkable reflectivity and emissivity for radiative cooling, among the best performance compared with other PDRC materials reported in the literature (Figure 2i; Tables S1 and S2, Supporting Information). Besides, the MFC/PCC composites exhibit notable mechanical enhancement with increasing PCC content. As the PCC loading increases from 60 to 70 wt.%, the tensile strength and elongation at break improve by 131.3% and 95.6%, respectively. Further increasing the PCC content from 70 to 80 wt.% results in additional improvements of 31.4% and 41.5%, respectively (Figure 2g). A significant performance trade-off exists between the PCC content and mechanical performance: when the PCC content is more than or equal to 80 wt.%, insufficient skeletal support leads to a significant decline in mechanical properties; when the PCC content is less than or equal to 60%, the latent heat is relatively small, which makes the phase change cooling performance insignificant. Based on this conflicting balance, this study ultimately determined 70 wt.% PCC (PCC/MFC = 7:3) as the optimal ratio. With such PCC content, the MFC/PCC-60 composite (with 70 wt.% PCCs) demonstrates substantial flexibility, it can be bent and twisted into various shapes (Figure S12, Supporting Information).

Given the significant influence of density and latent heat on the phase change cooling power (P_{PCC}), both the latent heat and density were measured. The differential scanning calorimetry (DSC) curve reveals that PCC has a high melting enthalpy of 201.7 J g^{-1} (Figure S13, Supporting Information). The MFC/PCC-60 composite still has a high latent heat of 132.1 J g^{-1} (Figure 2h), which is a significantly high value in homogeneous RPHC composites (Table S1, Supporting Information), due to the high content (70.0%) of PCCs. The high latent heat endows the MFC/PCC-60 with excellent phase change cooling performance.

When the MFC/PCC-60 composite was put on a heating stage at ≈60 °C (Figure S14, Supporting Information), the MFC/PCC-60 composite exhibited a gentle temperature rise (38–42 °C) during heating, while MFC-60 showed no obvious decay in the whole process. The maximum temperature difference between MFC-60 and MFC/PCC-60 could reach more than 10.0 °C at 54 s. The gradual rise of MFC/PCC-60 corresponds to the phase change process of absorbing heat, which reveals its great potential to improve cooling power based on traditional radiative cooling methods. In addition, due to the excellent encapsulation integrity of the microcapsules, the latent heat of MFC/PCC-60 decreased only slightly after 200 solid-liquid phase change cycles, demonstrating excellent long-term cycling stability (Figure S15, Supporting Information). These results highlight the effective thermal management capabilities of the MFC/PCC composite, validating its potential for advanced cooling applications.

2.3. Cooling Performance Assessment of MFC/PCC Composite

The remarkable optical and phase change properties of MFC/PCC-60 equip itself with the great potential to achieve hybrid subambient cooling. We conducted continuous cooling measurements from 7:00 on July 12th to 7:00 on July 13th, 2023, under clear sky conditions in Wuhan, which is in the central part of China and is a typical city with a subtropical monsoon climate type. To minimize conductive heat transfer, the samples were insulated with polystyrene (PS) foam, which was then covered with reflective foil to reduce solar absorption and further shielded with polyethylene (PE) film to reduce heat convection (**Figure 3a**). Temperature variations were monitored using thermocouples attached to the underside of each sample, along with concurrent measurements of ambient air temperature and solar irradiance (Figure 3b).

The results highlight the advantages of incorporating PCCs and utilizing a hierarchical structure in MFC/PCC composite for enhancing cooling performance. Across all samples, temperature increases were slow when solar irradiance was below 200 W m^{-2}. Afterward, as solar irradiance intensified, both ambient and sample temperatures rose rapidly. Although there is a significant difference in solar reflectivity between MFC/PCC-dry and MFC-60, their temperature rise curves during the morning heating phase (08:00–09:00) are highly similar. This is because the PCC melting process in MFC/PCC-dry absorbs a large amount of latent heat, effectively delaying its own temperature rise, thereby fully demonstrating the excellent thermal management capabilities of PCM. However, after the phase change process concludes, the low solar reflectivity of MFC/PCC-dry becomes a notable drawback, as it absorbs a large amount of solar radiation, causing its temperature to rise rapidly and significantly exceed that of MFC-60. By midday, when solar irradiance peaked at ≈1000 W m^{-2}, ambient temperatures reached a maximum of 68.1 °C. The MFC-dry, lacking PCCs and structural adjustments, exhibited a peak temperature of 71.6 °C. This substantial temperature rise in MFC-dry is attributed to its dense layered structure, which results in low reflectivity (< 0.4, Figure S16, Supporting Information) and significant solar energy absorption, leading to consistently higher temperatures. On average, the temperature of MFC-dry was 4.8 °C higher than the ambient temperature. In contrast, MFC-60, which incorporated water to optimize the microstructure, demonstrated notably enhanced cooling performance. Owing to high solar reflectivity and elevated MIR emissivity, MFC-60 effectively maintained temperatures significantly lower than ambient levels, achieving a peak temperature of 54.2 °C and an average temperature of 6.8 °C lower than the ambient conditions.

The introduction of PCCs into the MFC matrix further enhanced cooling capabilities. MFC/PCC-dry consistently maintained lower temperatures than MFC-dry, and MFC/PCC-60 outperformed MFC-60. On average, the addition of PCCs resulted in temperature reductions of 1.8 and 3.3 °C, respectively (Figure 3c). Furthermore, the combination of phase change processes and hierarchical structure in MFC/PCC-60 led to a significant improvement in cooling performance, achieving a temperature reduction of 12.4 °C below ambient at midday and an average cooling effect of 10.1 °C from 8:00 a.m. to 6:00 p.m., both of which are remarkable values. These findings underscore the efficacy of RPHC as an advanced cooling strategy. More importantly, under conditions of dynamic changes in solar radiation heat flux, PPC achieves dynamic regulation of its cooling capacity through its reversible phase change process. During the morning when solar radiation intensifies, the ambient temperature rises significantly. At this time, PPC absorbs latent heat through phase change, effectively slowing its own temperature rise rate and thereby avoiding thermal shock caused by sudden temperature increases. During the afternoon when solar radiation rapidly decreases, the ambient

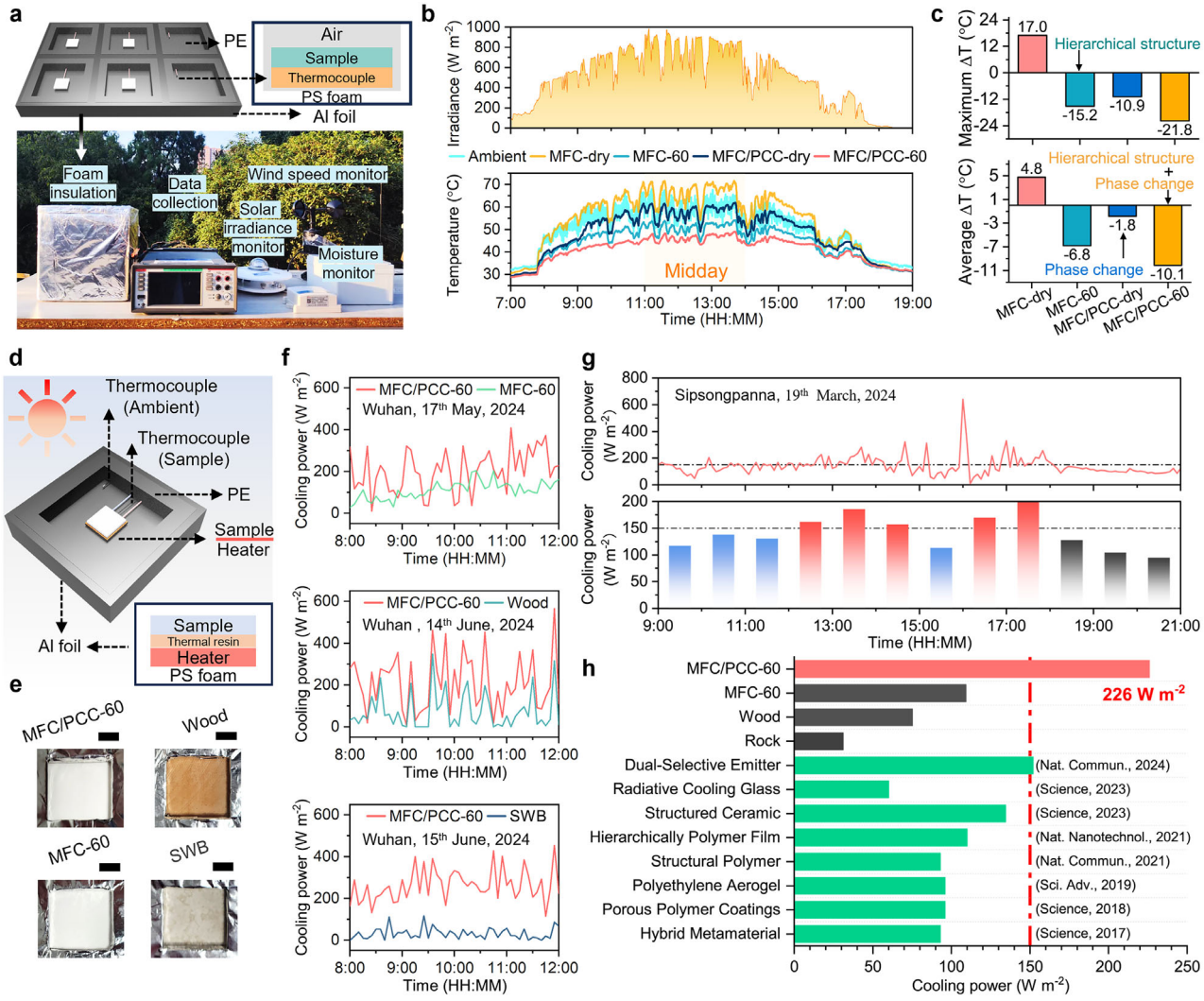

Figure 3. Cooling performance assessment of MFC/PCC composite. a) Experimental setup for the subambient cooling characterization. b) Solar intensity and sample temperatures measured in Wuhan (China, July 12th, 2023). c) Maximum and average temperature differences (ΔT) of samples compared with the ambient environment. d) Experimental setup for characterizing cooling power. e) The picture of samples (Scale bar: 20 mm). f) The cooling power of MFC/PCC-60, MFC-60, wood, and SWB in Wuhan (China, May 17th, 2024, June 14th, 2024, and June 15th, 2024). g) The cooling power curve and average cooling power each hour in Sipsongpanna (China, March 19th, 2024). h) Cooling power comparison of different reported PDRC materials with MFC/PCC-60.

temperature drops sharply. At this point, PPC undergoes a reverse phase change and releases latent heat, maintaining its own temperature relatively constant, thereby effectively buffering the cold shock caused by the sudden drop in ambient temperature and the continuous effect of radiative cooling. These findings indicate that integrating PCM with radiative cooling technology is a highly adaptive solution for addressing dynamic environmental changes and achieving efficient daytime cooling.

The cooling power of MFC/PCC-60 in Wuhan (China) was measured, using MFC-60 and two typical building materials (stone wool board (SWB), wood) as control samples (Figure 3d,e; optical properties of SWB and wood: Table S3, Supporting Information). To measure cooling power, a heater enclosed by an infrared-transparent polyethylene (PE) film was put beneath each sample, the heater would generate heat once the temperature differential exceeded 0.5 °C to compensate for the cooling power, with output recorded at the interval of 0.21 s.

In three separate tests, the solar irradiance, wind speed as well as humidity were collected (Figures S17–S19, Supporting Information). At peak solar intensities of approximately 850, 900, and 850 W m^{-2}, the average cooling powers of MFC/PCC-60 are 202, 212, and 264 W m^{-2}, respectively, while the average cooling powers of MFC-60, wood, and stone wool board (SWB) are 109, 75, and 31 W m^{-2}, respectively (Figure 3f). The MFC/PCC-60 consistently maintained cooling power (average cooling power = 226 W m^{-2}) beyond the power limit (≈150 W m^{-2}) of traditional radiative cooling, where the typical SWB and wood only have lower cooling power compared to MFC-60 with high reflectivity and emissivity. Beyond Wuhan (China), we assessed the cooling performance of the MFC/PCC-60 in Sipsongpanna (China), which is

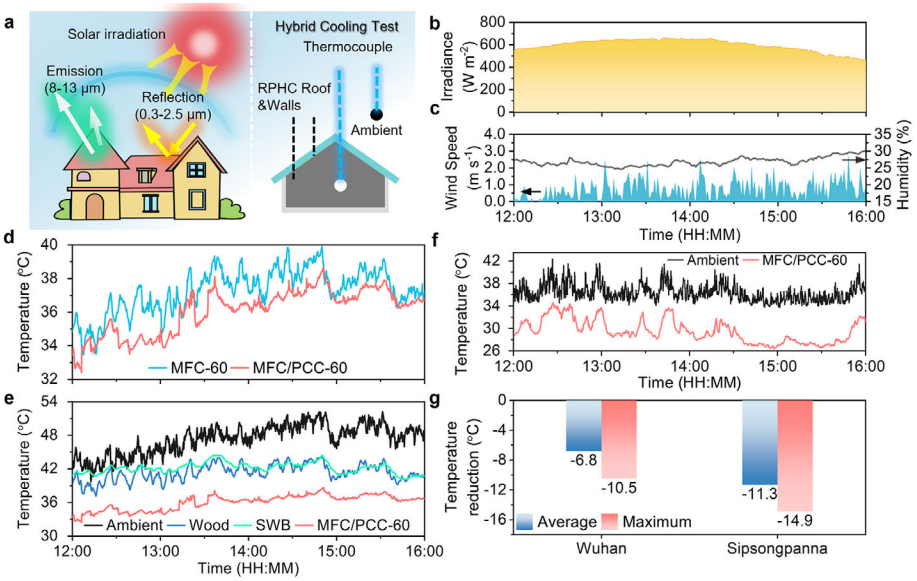

Figure 4. Cooling performance of MFC/PCC-60 as the roof and walls on a simulated house in an outdoor environment. a) Schematic of the basic principles of MFC/PCC-60 and setup of cooling performance characterizations. b) Solar intensity in Sipsongpanna (China, March 16th, 2024). c) Wind speed and relative humidity in Sipsongpanna (China, March 16th, 2024). d) Temperatures of MFC-60 and MFC/PCC-60 measured in Sipsongpanna (China, March 16th, 2024). e) Temperatures of Wood, SWB, MFC/PCC-60 and ambient condition measured in Sipsongpanna (China, March 16th, 2024). f) The temperatures of MFC/PCC-60 and ambient environment measured in Wuhan (China, September 23rd, 2024). g) The subambient cooling performances of MFC/PCC-60 in Wuhan (China) and Sipsongpanna (China).

a typical city with tropical monsoon rainforest climate type in the subtropics to further validate its cooling performance (Figure 3g). With a solar intensity reaching up to ≈700 W m^{-2} and the temperature difference curve is present in Figure S20 (Supporting Information), the MFC/PCC-60 achieved cooling power exceeding ≈150 W m^{-2} for 5 hours in daytime with the solar irradiance less than 700 W m^{-2}, the validation underscores the engineered MFC/PCC's capability to meet and exceed the demands for high-efficiency daytime cooling, crucial for addressing escalating energy demands associated with cooling in diverse climatic regions. Previous works concerning the cooling power based on radiative cooling and radiative-phase change hybrid cooling are summarized (Figure 3h; Table S1, Supporting Information). The cooling power value of MFC/PCC-60 is much higher than these reported works based on radiative cooling and radiative-phase change hybrid cooling, showing great potential in cooling applications.

2.4. Energy-Saving Evaluation of MFC/PCC

To evaluate the potential of the MFC/PCC composite, a simulated house with MFC/PCC-60 roof and walls was constructed and exposed to direct sunlight in both Sipsongpanna (China) and Wuhan (China) (**Figure 4a**; Figure S21, Supporting Information). Control structures were similarly constructed using MFC-60, stone wool board (SWB), and wood. A thermocouple monitored the internal air temperature within the enclosed structure, while external atmospheric temperature variations were recorded. The solar irradiance, wind speed, and humidity were provided in Figure 4b,c. As sunlight intensity increases, the internal temperatures of the house with varying roofs and walls increase simultaneously (Figure 4d). Under solar irradiance below 700 W m^{-2}, the inner temperature of the house built by MFC-60 composite reaches as high as 40 °C, consistently higher than that of MFC/PCC-60. Additionally, the houses with the wood and SWB materials simultaneously own the high inner temperatures, which are more than 5 °C higher than that of MFC/PCC-60 (Figure 4e). Moreover, the cooling performance of MFC/PCC-60 is more than 11.3 °C compared with ambient temperature, showing excellent cooling performance of MFC/PCC-60. The results are consistent with the optical and cooling power characterization.

To verify the widespread applicability of the cooling performance of MFC/PCC-60, the characterization is simultaneously conducted in Wuhan (China, Figure 4f). With the solar irradiance peaks at ≈700 W m^{-2}, the house with the MFC/PCC-60 roof and walls has a temperature always lower than the ambient temperature, and the average cooling temperature reaches as high as 11.3 °C (Figure 4g). These results collectively demonstrate the exceptional cooling ability of the MFC/PCC-60 composite, leveraging enhanced reflectivity through structure engineering and high latent heat to optimize cooling performance in real-world applications.

To evaluate the sustainability potential of MFC/PCC composites, we conduct an energy consumption simulation to quantify the associated energy savings and carbon emission reductions by integrating the MFC/PCC composites onto building roofs and walls of a two-floor mall (total air-conditioned area: 1608.58 m^2, Figure S22, Supporting Information). Annual cooling energy reductions across 104 Chinese cities were calculated, with the average savings for each province shown in **Figure 5a** (Table S4, Supporting Information). The energy savings in 12 climatically representative provinces (Figure 5b) and their respective savings ratios (Figure 5c) illustrate the MFC/PCC composite's

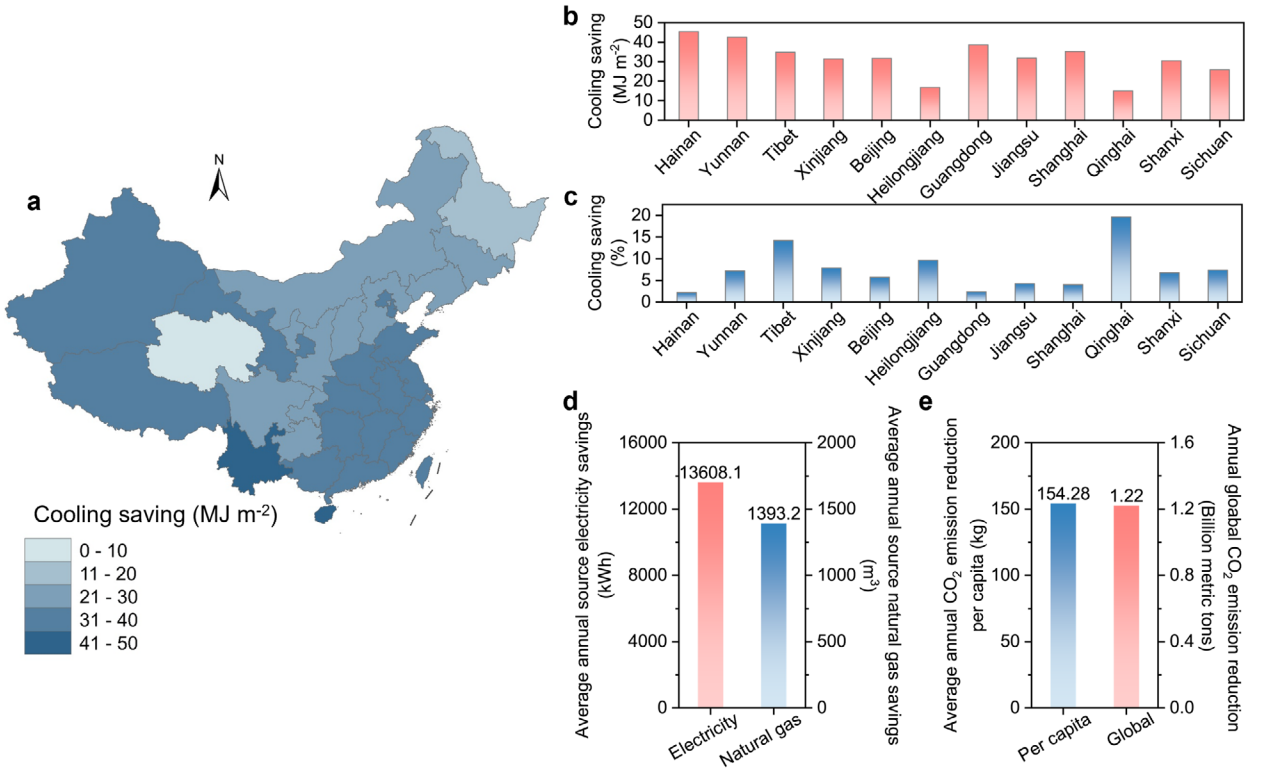

Figure 5. Modeling energy savings by covering MFC/PCC-60 composite on the roofs and external walls of a mall. a) Total predicted cooling energy saving ratios of two-floor malls extended for all Chinese cities based on local climate zones. b) Total cooling energy savings per year among 12 cities. c) Total cooling energy savings percentage per year among all 12 cities. d) Predicted average annual source electricity and source natural gas savings. e) Predicted average annual CO_2 emission reduction per capita and globally.

energy-saving capabilities. In terms of energy saving, Hainan and Yunnan (close to the equator) with hot weather have more energy saving, which reaches as high as 45.4 and 42.5 MJ m^{-2}. The energy savings of Xinjiang and Tibet in eastern China are also relatively high, exceeding 30.0 MJ m^{-2}, mainly because the cooling demand in these places is also relatively high in summer. The climate in the north is colder, such as Heilongjiang and Beijing, and is generally cold, so the energy saving is relatively low. The Guangdong Province, Jiangsu Province, and Shanghai also save cooling energy of more than 30.0 MJ m^{-2} due to low latitude and following high summer cooling demands. Interestingly, Qinghai Province, though cooler due to its high altitude, exhibited high energy-saving efficiency (over 15%) due to lower total energy demands for cooling. In contrast, the energy saving rate in coastal areas is relatively low, in the range of 0–5%, mainly because the cooling capacity is relatively high.

Overall, there is a trend that the absolute value of energy saving is high in hot areas, but the energy saving efficiency is reduced. It is worth mentioning that after installing RPHC composites, except for the three northeastern provinces and Qinghai, most of the actual energy savings can reach more than 20 MJ m^{-2}. At the same time, the energy-saving efficiency in more than two-thirds of the country exceeds 5%, both of which are remarkable values.[42] Nationally, an overall energy-saving efficiency of 4.4% indicates the promising potential of MFC/PCC composites for energy saving.

In addition, we transformed the energy saving of the simulated building each year into source and energy saving and source of natural gas, the results are shown in Figure 5d,e. The MFC/PCC composite acting as the cover of the roofs and external walls can save 13608.1 kWh of source power and 1393.2 m^3 of natural gas each year for the two-floor mall. According to the International Energy Agency, this is equivalent to reducing 8164 kg of greenhouse gas emissions and 154.28 kg per capita greenhouse gas emissions. According to the world population in 2023, we roughly estimate that it is equivalent to reducing the emissions of 1.22 billion tons of greenhouse gas, which is equivalent to a decrease of 3.3% (the total amount of greenhouse gas emissions in 2023 was 37.4 billion tons). The above results show that the RPHC composite is of great significance for energy conservation and emission reduction.

3. Conclusion

In summary, this study introduces an efficient water pre-removal freeze-drying method to optimize the structure and cooling performance of a porous RPHC composite by integrating PCCs within an MFC matrix. Combining the water content adjustment to tune the structure of MFC/PCC, the addition of PCCs substantially enhances light scattering and efficiently absorbs excess heat, facilitating superior cooling performance. The resulting MFC/PCC composite exhibits remarkable properties, with high solar reflectivity (0.969), emissivity (0.958), latent heat

capacity (132.1 J g^{-1}), and comparable density (0.652 g cm^{-3}), achieving an exceptional cooling power of 226 W m^{-2}, which surpasses the conventional limits of radiative cooling. Additionally, the MFC/PCC composite demonstrated an average temperature reduction of 10.1 °C below ambient. This innovative RPHC composite offers significant environmental benefits, with the potential to reduce 4.4% of the building's cooling energy consumption and global carbon emissions by approximately 1.22 billion metric tons annually. Furthermore, the hybrid cooling composite may propel advancements in passive cooling applications, including the thermal management of buildings, electronic devices, vehicles, and especially outdoor environments. Outdoor tasks such as cold chain transportation and personal thermal management can benefit from the MFC/PCC's cooling capabilities, which are crucial for maintaining low temperatures. Importantly, the entire hybrid cooling process employed in this composite requires no additional chemicals, ensuring a fully environmentally friendly production, and achieving emission reductions through energy savings in cooling applications.

4. Experimental Section

Materials: Microfibrillated cellulose (MFC) aqueous dispersion was purchased from Qihong Technology Co., Ltd. (Guilin, China). Melamine powder, formaldehyde, and n-docosane were obtained from Sinopharm Chemical Reagent Co., Ltd. (Shanghai, China) and Aladdin Biochemical Technology Co., Ltd. (Shanghai, China), respectively. Styrene-sodium maleic anhydride copolymer (SMA) was obtained from Wuzhi Zhihui Technology Co., Ltd. (Henan, China).

Material Preparation: *Phase Change Capsules*: Melamine powder, formaldehyde solution, and deionized water were mixed in a three-necked flask. The pH of the mixture was adjusted to 8.5 using triethanolamine, and the solution was stirred at 70 °C for 60 minutes to form a melamine-formaldehyde prepolymer. Concurrently, n-docosane and a 4.26 wt.% SMA solution were emulsified using a high-speed homogenizer (IKA T-25 Ultra Turrax) at 9000 rpm and 60 °C for 45 minutes, resulting in a stable emulsion. The melamine-formaldehyde prepolymer was then added dropwise to this emulsion under mechanical stirring at 500 rpm for 30 minutes. The reaction mixture was cooled to room temperature, yielding a microcapsule dispersion.

MFC/PCC Composite: MFC and PCCs were mixed in a 3:7 weight ratio. The mixture was subjected to vacuum filtration to remove water. Once the water filtration ratio reached the desired level, the sample was freeze-dried and designated as MFC/PCC-X, where X represents the water filtration ratio (e.g., MFC/PCC-60 for 60 wt.% water filtration).

Characterization: Reflectivity was measured using a UV–vis–NIR spectrophotometer (Shimadzu UV-3600, Japan) in integrating sphere mode, with polytetrafluoroethylene as the back plate, scanning from 200 to 2500 nm at 1 nm s^{-1}. Emissivity was determined with a Fourier transform infrared spectrometer (Thermo Scientific FT-IR Nicolet iS50R), using a mid-infrared integrating sphere accessory to scan from 2.5 to 14.8 µm. Infrared spectra were obtained with a Fourier transform infrared spectrometer (Bruker VERTEX 70) in ATR mode from 600 to 4000 cm^{-1}. The morphologies and microstructures were observed with a field emission scanning electron microscope (SEM, Sirion 2000, FEI). Differential scanning calorimetry (DSC) data were collected using a DSC25 (TA Instruments, USA) with a heating and cooling rate of 1 °C min^{-1} for PCC and MFC/PCC composites, and 10 °C min^{-1} for cycling tests from 0 to 60 °C. Temperature data were recorded every 10 seconds with a Keithley 7700 data logger. Solar irradiation was measured with a GTBQ solar radiation sensor (GTBQBA2500, Rika, China), while humidity and wind speed were recorded using a temperature and humidity sensor (QRAIOA-EBA2000, Rika, China) and a wind speed sensor (FWSCAA1500, Rika, China), respectively. The accelerated thermal cycling test was tested via the temperature-control chamber (KSON KTHB-415TBS, China) between 10 and 90 °C.

Pore Size Distribution: The pore size distribution was determined using a mercury intrusion porosimeter. The dried and evacuated sample was first tested at low pressure to record the initial mercury intrusion volume. Pressure was then gradually increased, and the cumulative intrusion volume was measured at each pressure point. The critical pore size was calculated from the applied pressure using the Washburn equation. The cumulative mercury volume–pore size curve was obtained, and the pore size distribution was derived from the derivative of this curve.

Cooling Test: Field tests were conducted in Wuhan (China) and Sipsongpanna (China). To accurately assess the cooling performance of the RPHC, samples (20 mm × 20 mm × 2 mm) were placed in a foamed polystyrene groove lined with tin foil. Two K-type thermocouples connected to a Keithley data logger were affixed to the sample's bottom and in the corner of chamber, respectively. The groove was sealed with a low molecular weight polyethylene film, and solar irradiation, humidity, and wind speed were recorded using meteorological instruments.

For power testing, a polyimide heating plate was placed beneath the sample. A K-type thermocouple was positioned between the sample (60 mm × 60 mm × 16 mm) and the heating plate, with an additional sensor installed in the corner in the chamber. A control feedback system maintained the sample temperature in alignment with the ambient temperature, and the heating plate power was adjusted to match the sample's rated cooling power.[12] The cooling effect was also tested without a windshield or solar radiation shield. The samples and comparison materials were housed in sealed boxes, with temperature measured by inserting a K-type thermocouple into the box.

Energy-Saving Calculation: Energy consumption simulations were performed using DEST2.0 software for a two-floor mall measuring 54.62 meters in length and 17.92 meters in width, with a total air-conditioned area of 1608.58 m^2 (Figure S22, Supporting Information). The building's orientation is north-facing, with a window-to-wall ratio of 0.12 on both the south and north facades. Building envelope parameters were set according to the "Public Building Energy Saving Design Standard DB37 5155-2019": exterior wall heat transfer coefficient at 0.609 W $m^{-2}\cdot K^{-1}$, roof heat transfer coefficient at 0.595 W $m^{-2}\cdot K^{-1}$, exterior window heat transfer coefficient at 3.0 W $m^{-2}\cdot K^{-1}$, and shading coefficient at 0.8. The HVAC system comprises a fan coil combined with a fresh air system for heating and cooling. Indoor temperatures are set at 26 °C in summer and 18 °C in winter. Outdoor meteorological data were sourced from typical annual data in DEST2.0, including hourly temperature, relative humidity, wind direction, wind speed, and solar radiation. The reflectivity and emissivity of the building's exterior surfaces were initially set at 0.50 and 0.85, respectively. This MFC/PCC composite significantly reduces solar heat absorption, lowering cooling demands. By comparing models with and without the MFC/PCC composite, annual heating and cooling energy consumption was calculated for 104 cities across China. An energy-saving map was generated and extrapolated to adjacent areas. The annual energy savings were normalized by the total floor area of the mall (1608.58 m^2).

Supporting Information

Supporting Information is available from the Wiley Online Library or from the author.

Acknowledgements

This work was supported by the National Natural Science Foundation of China (Grant No. 52173036, Grant No. 22475007), the National Key Technology R&D Program of China (Grant No. 2020YFB1709301, Grant No. 2020YFB1709304), the Fundamental Research Funds for Central Universities (Grants No. 2021XXJS035).

Conflict of Interest

The authors declare no conflict of interest.

Author Contributions

X.H. and B.Q. contributed equally to this work. X.H., B.Q., X.L., Y.P., and J.Q. conceived the idea. Y.P., X.L., and J.Q. supervised the project. X.H., B.Q., G.L., Z.S., and Y.D. designed and carried out all of the experiments. Z.S. and X.Z. performed the optical modeling. X.H., B.Q., X.L., J.L., Y.P., and J.Q. wrote the paper. All of the authors discussed the results and assisted in the writing of the paper.

Data Availability Statement

The data that support the findings of this study are available from the corresponding author upon reasonable request.

Keywords

bioinspired, carbon neutrality, hybrid cooling, phase change, radiative cooling

Received: June 10, 2025
Revised: October 9, 2025
Published online:

[1] D. García-León, A. Casanueva, G. Standardi, A. Burgstall, A. D. Flouris, L. Nybo, *Nat. Commun.* **2021**, *12*, 5807.
[2] Y. Zhu, H. Luo, C. Yang, B. Qin, P. Ghosh, S. Kaur, W. Shen, M. Qiu, P. Belov, Q. Li, *Light Sci. Appl.* **2022**, *11*, 122.
[3] Y. Peng, J.-C. Lai, X. Xiao, W. Jin, J. Zhou, Y. Yang, X. Gao, J. Tang, L. Fan, S. Fan, Z. Bao, Y. Cui, *Proc. Natl. Acad. Sci.* **2023**, *120*, 2300856120.
[4] M. Ono, K. Chen, W. Li, S. Fan, *Opt. Express* **2018**, *26*, A777, https://doi.org/10.1364/OE.26.00A777.
[5] X. Ao, B. Li, B. Zhao, M. Hu, H. Ren, H. Yang, J. Liu, J. Cao, J. Feng, Y. Yang, Z. Qi, L. Li, C. Zou, G. Pei, *Proc. Natl. Acad. Sci. USA* **2022**, *119*, 2120557119, https://doi.org/10.1073/pnas.2120557119.
[6] W. Su, P. Cai, R. Kang, L. Wang, G. Kokogiannakis, J. Chen, L. Gao, A. Li, C. Xu, *Appl. Energy* **2022**, *322*, 119457, https://doi.org/10.1016/j.apenergy.2022.119457.
[7] M.-C. Huang, M. Yang, X.-J. Guo, C.-H. Xue, H.-D. Wang, C.-Q. Ma, Z. Bai, X. Zhou, Z. Wang, B.-Y. Liu, Y.-G. Wu, C.-W. Qiu, C. Hou, G. Tao, *Prog. Mater. Sci.* **2023**, *137*, 101144, https://doi.org/10.1016/j.pmatsci.2023.101144.
[8] R. Liu, S. Wang, Z. Zhou, K. Zhang, G. Wang, C. Chen, Y. Long, *Adv. Mater.* **2025**, *37*, 2401577.
[9] A. P. Raman, M. A. Anoma, L. Zhu, E. Rephaeli, S. Fan, *Nature* **2014**, *515*, 540.
[10] X. Yin, R. Yang, G. Tan, S. Fan, *Science* **2020**, *370*, 786.
[11] Y. Zhai, Y. Ma, S. N. David, D. Zhao, R. Lou, G. Tan, R. Yang, X. Yin, *Science* **2017**, *355*, 1062, https://doi.org/10.1126/science.aai7899.
[12] T. Li, Y. Zhai, S. He, W. Gan, Z. Wei, M. Heidarinejad, D. Dalgo, R. Mi, X. Zhao, J. Song, J. Dai, C. Chen, A. Aili, A. Vellore, A. Martini, R. Yang, J. Srebric, X. Yin, L. Hu, *Science* **2019**, *364*, 760, https://doi.org/10.1016/j.msea.2018.02.027.
[13] D. Li, X. Liu, W. Li, Z. Lin, B. Zhu, Z. Li, J. Li, B. Li, S. Fan, J. Xie, J. Zhu, *Nat. Nanotechnol.* **2021**, *16*, 153, https://doi.org/10.1038/s41565-020-00800-4.
[14] T. Wang, Y. Wu, L. Shi, X. Hu, M. Chen, L. Wu, *Nat. Commun.* **2021**, *12*, 365, https://doi.org/10.1038/s41467-020-20646-7.
[15] J. Mandal, Y. Fu, A. C. Overvig, M. Jia, K. Sun, N. N. Shi, H. Zhou, X. Xiao, N. Yu, Y. Yang, *Science* **2018**, *362*, 315.
[16] X. Wu, J. Li, F. Xie, X. Wu, S. Zhao, Q. Jiang, S. Zhang, B. Wang, Y. Li, D. Gao, R. Li, F. Wang, Y. Huang, Y. Zhao, Y. Zhang, W. Li, J. Zhu, R. Zhang, *Nat. Commun.* **2024**, *15*, 815, https://doi.org/10.1038/s41467-024-45095-4.
[17] J. Ma, F. Zeng, X. Lin, Y. Wang, Y. Ma, X. Jia, J. Zhang, B. Liu, Y. Wang, H. Zhao, *Science* **2024**, *385*, 68.
[18] S. Fan, W. Li, *Nat. Photonics* **2022**, *16*, 182.
[19] D. Zhao, A. Aili, Y. Zhai, S. Xu, G. Tan, X. Yin, R. Yang, *Appl. Phys. Rev.* **2019**, *6*, 021306.
[20] H. Zhang, S. Zhou, H. Liu, Z. Qian, X. Wang, *Adv. Funct. Mater.* **2024**, *34*, 2408269, https://doi.org/10.1002/adfm.202408269.
[21] J. Song, Z. Zheng, S. Zhou, T. Shi, H. Liu, X. Wang, *ACS Appl. Mater. Interfaces* **2025**, *17*, 35409, https://doi.org/10.1021/acsami.5c03806.
[22] S. Wang, M. Wu, H. Han, R. Du, Z. Zhao, W. Liu, S. Wu, R. Wang, T. Li, *Adv. Energy Mater.* **2024**, *14*, 2402667, https://doi.org/10.1002/aenm.202402667.
[23] G. Wang, Z. Tang, Y. Gao, P. Liu, Y. Li, A. Li, X. Chen, *Chem. Rev.* **2023**, *123*, 6953, https://doi.org/10.1021/acs.chemrev.2c00572.
[24] B. Gu, G. Li, Q. Zhang, H. Pan, M. Duan, L. Weng, D. Zhao, *Adv. Funct. Mater.* **2025**, *35*, 2412089, https://doi.org/10.1002/adfm.202412089.
[25] W. Liu, Y. Dong, M. Li, H. Liu, X. Wang, *Adv. Funct. Mater.* **2025**, 13665, https://doi.org/10.1002/adfm.202513665.
[26] M. Yang, H. Zhong, T. Li, B. Wu, Z. Wang, D. Sun, *ACS Nano* **2023**, *17*, 1693, https://doi.org/10.1021/acsnano.2c11916.
[27] Z. Zhu, A. Bashir, X. Wu, C. Liu, Y. Zhang, N. Chen, Z. Li, Y. Chen, X. Ouyang, D. Chen, *Adv. Funct. Mater.* **2025**, *35*, 2416111, https://doi.org/10.1002/adfm.202416111.
[28] W. Su, R. Kang, P. Cai, M. Hu, G. Kokogiannakis, J. Darkwa, J. Chen, S. Xu, L. Wang, *Sol. Energy Mater. Sol. Cells* **2023**, *251*, 112125, https://doi.org/10.1016/j.solmat.2022.112125.
[29] S. Tao, Q. Wan, Y. Xu, D. Gao, Z. Fang, Y. Ni, L. Fang, C. Lu, Z. Xu, *Energy Build.* **2023**, *288*, 113031, https://doi.org/10.1016/j.enbuild.2023.113031.
[30] L. Wang, Z. Yang, S. Zhou, H. Liu, X. Wang, *Chem. Eng. J.* **2025**, *521*, 166520, https://doi.org/10.1016/j.cej.2025.166520.
[31] Y. Zhu, R. Haghniaz, M. C. Hartel, S. Guan, J. Bahari, Z. Li, A. Baidya, K. Cao, X. Gao, J. Li, Z. Wu, X. Cheng, B. Li, S. Emaminejad, P. S. Weiss, A. Khademhosseini, A. Breathable, *Adv. Mater.* **2023**, *35*, 2209300, https://doi.org/10.1002/adma.202209300.
[32] A. Leroy, B. Bhatia, C. C. Kelsall, A. Castillejo-Cuberos, M. Di Capua H, L. Zhao, L. Zhang, A. M. Guzman, E. N. Wang, *Sci. Adv.* **2019**, *5*, aat9480.
[33] K. Lin, S. Chen, Y. Zeng, T. C. Ho, Y. Zhu, X. Wang, F. Liu, B. Huang, C. Y.-H. Chao, Z. Wang, C. Y. Tso, *Science* **2023**, *382*, 691.
[34] X. Wu, J. Li, Q. Jiang, W. Zhang, B. Wang, R. Li, S. Zhao, F. Wang, Y. Huang, P. Lyu, Y. Zhao, J. Zhu, R. Zhang, *Nat. Sustain.* **2023**, *6*, 1446.
[35] S. Shi, C. Valenzuela, Y. Yang, Y. Liu, B. Li, L. Wang, W. Feng, *Chin. J. Chem.* **2023**, *41*, 2611, https://doi.org/10.1002/cjoc.202300282.
[36] U. Schulz, C. Präfke, P. Munzert, C. Gödeker, N. Kaiser, *Opt. Mater. Express* **2011**, *1*, 101, https://doi.org/10.1364/OME.1.000101.
[37] M. Ma, Q. Ai, M. Xie, *Optik* **2022**, *249*, 168277, https://doi.org/10.1016/j.ijleo.2021.168277.
[38] X. Zhao, T. Li, H. Xie, H. Liu, L. Wang, Y. Qu, S. C. Li, S. Liu, A. H. Brozena, Z. Yu, J. Srebric, L. Hu, *Science* **2023**, *382*, 684.
[39] L. Xiong, Y. Wei, C. Chen, X. Chen, Q. Fu, H. Deng, *Nat. Commun.* **2023**, *14*, 6129, https://doi.org/10.1038/s41467-023-41797-3.
[40] K. Weng, R. Qian, X. Xu, D. Zou, *Int. J. Heat Mass Transf.* **2024**, *234*, 126090, https://doi.org/10.1016/j.ijheatmasstransfer.2024.126090.
[41] T. Jiang, S. Chen, J. Xu, Y. Zhang, H. Fu, Q. Ling, Y. Xu, X. Chu, R. Wang, L. Hu, H. Li, W. Huang, L. Bian, P. Zhao, F. Wei, *Nat. Commun.* **2024**, *15*, 5460, https://doi.org/10.1038/s41467-024-49578-2.
[42] K.-Y. Chan, X. Shen, J. Yang, K.-T. Lin, H. Venkatesan, E. Kim, H. Zhang, J.-H. Lee, J. Yu, J. Yang, J.-K. Kim, *Nat. Commun.* **2022**, *13*, 5553.